A method for path calibration using regional and teleseismic broadband seismograms: Application to the 21 May 1997 Jabalpur, India earthquake (M_W 5.8)

Chandan K. Saikia

URS Group Inc, 566 El Dorado Street, Pasadena, CA 91101, USA

Regional seismograms can be used to retrieve source parameters from events too small to be seen teleseismically. The procedure is to invert P waves to obtain focal mechanism solutions for a suite of depths and model regional waveforms to constrain the source parameters. Regional crustal structures are refined so that they have the capability to generate regional phases, both in amplitude and absolute travel time. The calibrated regional models are then used to invert regional broadband seismograms of smaller earthquakes, not often recorded at teleseismic distances, for retrieval of depth, focal mechanism and seismic moment. In this paper, we demonstrate the applicability of this method using teleseismic and regional seismograms from the 22 May 1997 Jabalpur earthquake. This analysis indicated that the event occurred at a depth of 35 km and consisted of two seismic sources separated by 0.6 s. Using these source parameters we analysed the composition of significant phases, in particular the SP and sP_n phases observed on the regional seismograms of stations BHPL and BLSP, using the up-going and down-going wavefields from the source. The phase sP_n is a stable phase and is strong at stations NIL (Nilore in Pakistan) and LSA (Lhasa in China) located at about 12° away from the source.

Introduction

A number of studies have demonstrated that regional path calibration is essential for obtaining accurate locations of seismic events, especially at smaller magnitude (M_W < 5)[1-4]. More recent advancements have led to modelling of regional seismograms routinely in various regions, especially to yield seismic source parameters[5-10]. These methods were successfully used in calibrating regional path and locating seismic events in Pamir–Hindu-Kush

e-mail: Chandan_Saikia@urscorp.com

region[1,2,4], western Mediterranean and North Africa[11], the former Soviet Union[9], southern California[8,10] and central Asia[12]. Several recent studies[1,2,4] have illustrated that the locations in the monthly International Seismological Centre (ISC) and Preliminary Data Centre (PDE) bulletins are not always reliable for smaller events ($M_W \leq 4.5$). In particular, studies[1,2,4,13] have demonstrated that small events can be relocated by several tens of kilometres from their reported locations. The reason for the error in the ISC/PDE locations for the small events is that they are based on crustal models which do not consider the region-specific upper crust, including the other reasons such as the poor azimuthal coverage, poor arrival time picks because of the signal to noise ratio problem and lack of depth phase controls.

In this paper we review a systematic approach which can be used to calibrate regional crustal structure. The method requires modelling of teleseismic seismograms from a set of master events ($M_W \geq 5.5$) to establish accurate depth and focal mechanism. In turn, regional seismograms are modelled to refine the crustal structure so that various characteristics of regional phases can be adequately modelled. The absolute travel times of individual seismic phases, such as of P, S and surface waves, dispersive characteristics of surface waves and waveform features are the key features that are modelled to this end.
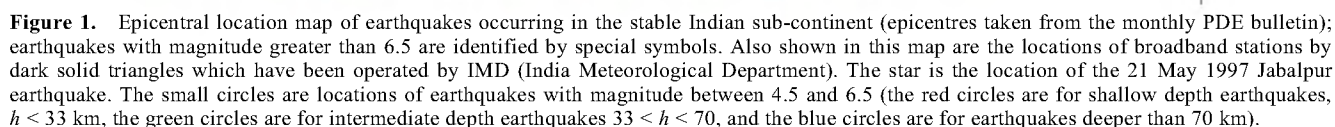
India is ideal for this approach since earthquakes are plentiful, especially along the Himalayan belt from north-west Pakistan in the west to eastern India along the Indo-Burma orogeny (Figure 1). A majority of the moderate-sized earthquakes are associated with the movement across the two major faults, namely the Main Boundary Thrust (MBT) and Main Central Thrust (MCT) fault, that extend along the entire Himalayan belt. Moderate-sized earthquakes occur less often in the seismically stable peninsular India, but have caused extensive damage. Of these, the earthquake of 21 May 1997 (shown by the solid star in Figure 1) occurred in the town of Jabalpur (origin time: 22 h 51 min 28.7 s, 23.083°N, 80.041°E, $h = 36$ km, $M = 5$, PDE) and killed at least 43 people, injured more than 1000, and left thousands homeless. It generated both

teleseismic and several regional seismograms[14,15], providing an ideal data set to illustrate methods that can be applied to calibrate various geological provinces in India, using broadband regional seismograms currently being archived at India Meteorological Department (IMD) from various Indian stations shown by triangles in Figure 1.

Modelling teleseismic waveforms of master events ($M_W \geq 5.5$)

The earthquakes selected for teleseismic modelling, which we call the master events, should be large enough, $M_W \geq 5.5$, so that they generate discernable depth phases, namely the pP and sP waves. Generally large events ($M_W > 6$) are recorded at many teleseismic stations, but they are problematic because their source process is generally complex and path calibration based on their regional seismograms can be a challenge, unless the source process is successfully deciphered. For moderate-sized earthquakes the source process is simple and often can be approximated with a simple source time function.

Modelling of teleseismic P and S wave data and their depth phases, i.e. the pP and sP phases, is dependent on the source and receiver region crustal structure, but is less sensitive to the details of regional waveguide. There are two popular approaches to model these seismograms. One of the approaches uses the generalized ray theory[5] in the range of 30° to 90°. The other approach uses the propagator-matrix technique[16] to propagate the wavefield from the source discontinuity through the source and receiver crustal structure. Geometrical spreading and $Q(t^*)$ effects are included for the teleseismic path. Unlike in the generalized ray approach in which the specified ray response is evaluated, this method computes the total wavefield. We developed a code modHSKL using this approach. In this paper we only discuss this latter method. This algorithm allows computation of synthetic responses for the three fundamental faults, namely the strike-slip, dip-slip and 45° dipping dip-slip faults. The seismic wavefield is propagated from the source discontinuity to the mantle and is convolved with the mantle response represented by Q (attenuation) and the geometrical spreading[17,18]. The resulting wavefield is allowed to propagate through the receiver crust to the surface. The code calculates distances, azimuths, travel times, angles of incidence at source and the free surface, including the geometrical spreading for the P and S waves, and their respective attenuation factors and uses the J–B travel-time table when necessary. The only input parameters needed to execute this algorithm are the earthquake and receiver locations, and the separate crustal models for the source and receiver region[19].

Figure 1. Epicentral location map of earthquakes occurring in the stable Indian sub-continent (epicentres taken from the monthly PDE bulletin); earthquakes with magnitude greater than 6.5 are identified by special symbols. Also shown in this map are the locations of broadband stations by dark solid triangles which have been operated by IMD (India Meteorological Department). The star is the location of the 21 May 1997 Jabalpur earthquake. The small circles are locations of earthquakes with magnitude between 4.5 and 6.5 (the red circles are for shallow depth earthquakes, $h < 33$ km, the green circles are for intermediate depth earthquakes $33 < h < 70$, and the blue circles are for earthquakes deeper than 70 km).

Teleseismic waveforms are inverted using Green's functions to obtain the best fitting source parameters by sweeping through the parameter space of the entire focal sphere. Depth is estimated by modelling the travel times of pP and sP phases relative to the P-wave onsets, and focal mechanism is determined by the amplitudes and polarities of these phases. For the code to perform optimally, the data and synthetic seismograms are aligned by maximizing the cross-correlation functions between data and synthetic seismograms[7,20].

The wavefields $(G_{w,q,v})$ of the fundamental faults are combined to yield vertical (W), radial (Q) and tangential (V) seismograms for any fault of arbitrary dip (δ), rake (λ) and strike (ϕ) as follows:

$$W(t,r,z,\delta,\lambda,\phi,AZ) = \sum_{j=1}^{3} G_{W_j}(t,r,z)\, A_j(\delta,\lambda,\phi,AZ),$$

$$Q(t,r,z,\delta,\lambda,\phi,AZ) = \sum_{j=1}^{3} G_{Q_j}(t,r,z)\, A_j(\delta,\lambda,\phi,AZ), \quad (1)$$

$$V(t,r,z,\delta,\lambda,\phi,AZ) = \sum_{j=4}^{5} G_{V_j}(t,r,z)\, A_j(\delta,\lambda,\phi,AZ),$$

where the indices $j = 1, 2, 3$ correspond to the wavefield produced by strike-slip, dip-slip, and $45°$ dipping dip-slip faults for the vertical and radial displacements, and indices $j = 4$ and 5 correspond to strike-slip and dip-slip faults for tangential displacements. A_j's are defined in terms of the vector $n(n_1, n_2, n_3)$ normal to the fault and the direction of the slip $f(f_1, f_2, f_3)$ as

$$A_1 = (f_1 n_1 - f_1 n_1)\cos(2Az) + (f_1 n_2 + f_2 n_1)\sin(2Az),$$

$$A_2 = (f_1 n_3 + f_3 n_1)\cos(Az) + (f_2 n_3 + f_3 n_2)\sin(Az),$$

$$A_3 = f_3 n_3, \quad (2)$$

$$A_4 = (f_1 n_1 - f_2 n_2)\sin(2Az) - (f_1 n_2 + f_2 n_1)\cos(2Az),$$

$$A_5 = (f_1 n_3 + f_3 n_1)\sin(Az) - (f_2 n_3 + f_3 n_2)\cos(Az),$$

where Az is the azimuth of the station measured from the north, and n_is and f_is are expressed in terms of δ, λ, ϕ as

$$n_1 = -\sin\delta \sin\phi, \quad f_1 = \cos\lambda \cos\phi + \sin\lambda \cos\delta \sin\phi,$$

$$n_2 = +\sin\delta \cos\phi, \quad f_1 = \cos\lambda \sin\phi - \sin\lambda \cos\delta \cos\phi, \quad (3)$$

$$n_3 = -\cos\delta, \qquad f_3 = -\sin\lambda \sin\delta.$$

The above formulation is used to synthesize the wavefields in which the numerical values of A_js are calculated using n_i's and f_i's for a particular combination of δ, λ, ϕ, using eqs (2) and (3), and are used to combine the Green's functions G_{Wj}, G_{Qj} and G_{Vj} according to the eq. (1).

Application of teleseismic modelling method

In this section, we illustrate the above method by applying it to the 21 May 1997 (GMT) Jabalpur, central India earthquake. The main tectonic features of this epicentral region are confined to two faults, namely the Son Narmada north and Son Narmada south Faults[14,15]. In general, the seismic activity is very low in peninsular India and the faults are not often exposed at the surface or show very little evidence of deformation[21]. On the other hand, faults are surface exposed in many tectonically active regions along the northern and eastern boundaries of the Indian plate. Thus, waveform modelling of seismograms generated by earthquakes on faults with very little deformation or those buried under the Deccan basalts in the peninsular India becomes useful in delineating their tectonic orientations.

Following the earthquake, we assembled a large number of teleseismic seismograms from 28 usable broadband stations $(30° \leq \text{Å} \leq 90°)$ from the IRIS Data Management Centre (DMC) as well as from several other stations located at upper-mantle distances. The data were converted into Seismic Analysis Code (SAC, Lawrence Livermore Laboratory, Revision 6) format and the P onset was determined by visual inspection and marked (T1 marker). The seismograms were detrended and the ends tapered using a Hanning window before deconvolving the instrument response using the poles and zeroes which were also downloaded from the DMC. The north-south and east-west components were rotated to radial and tangential seismograms. Since only the P-wave seismograms were inverted in this study, we retained the vertical and radial seismograms for about 60 s following the P onset for the subsequent analysis.

Next we computed a set of Green's functions using modHSKL for all the teleseismic stations for a suite of focal depths from 5 to 40 km using a depth interval of 5 km. The crust model used for this calculation is presented in Table 1 and the details of the model are dis-

Table 1. Crustal structure used for stations BLSP, BHPL and HYB (taken from Singh et al.[15])

V_p (km/s)	V_s (km/s)	Thickness (km)	Density (g/cm^3)
Station BLSP			
5.8	3.60	13.8	2.88
6.4	3.76	24.9	2.98
7.91	4.58	–	3.28
Station BHPL			
5.8	3.50	13.8	2.88
6.3	3.76	24.9	2.98
7.91	4.45	–	3.28
Station HYB			
6.15	3.50	15.0	2.293
6.75	3.85	30.0	3.050
8.05	4.68	–	3.260

cussed later. The P wave onsets were also placed in these synthetic waveforms. We used these Green's functions to invert the vertical and radial observed P-wave seismograms for the best fitting focal mechanism solution and depth using the grid-search approach. For the grid-search technique to become optimal we constructed cross-correlation time series cross-correlating synthetic seismograms of the fundamental faults and cross-correlation time series by cross-correlating data with the fundamental fault seismograms. These cross-correlation time series were used to sweep through a suite of focal mechanisms with δ ranging from 5° to 90° using 5° interval, λ from − 180° to 180° and Ö from 0° to 360°, both with 15° intervals, to estimate the correlation functions at zero-alignment between the data and synthetic waveforms.

Figure 2 shows the agreement between data and synthetic seismograms for the best fitting focal mechanism and depth solution for the vertical and radial seismograms. The solid thick lines represent recorded data and the thin lines are the corresponding synthetic seismograms. The depth phases are marked by vertical lines. Each station name is given to the left of the vertical seismograms. The azimuth and epicentral distance, r, is given in degrees. Note that the various phases are modelled extremely well. For example, the agreement in the pP and sP depth phases to the data both in travel time and ampli-

tude is quite remarkable. The pP phase arrives sooner than the sP phase relative to the P waves and appears to exhibit a large variation in amplitude with azimuth. This variation is probably caused by the focal mechanism rather than the variation in the receiver structure, because this phase is strongly recorded at stations BGCA, CTAO, DBIC, KMBO, WRAB and SSE, and not at the other stations, and because we were able to model the observed amplitude variation in pP waves using the same structure for all stations. The mismatch between the data and synthetic pP seismograms at INCN and SSE is, however, caused probably by local effects beneath the two stations. The stations which have small amplitudes for the pP waves are ALE, ARU and KIV; the best fitting solution yields synthetic seismograms which are in agreement with observed seismograms at these stations.

In the teleseismic waveforms shown in Figure 2 there is a distinct second arrival immediately following the P-wave onset. Figure 3 a is a blow-up of the vertical component of the teleseismic P waves recorded at DBIC. The two pulses are clear in the first half cycle of the P onset. The peak of the second arrival is indicative of a second source which cannot be modelled otherwise and is delayed by about 1.0 s from the peak of the first source. Since the earthquake is deep (35 km), the second pulse cannot be associated with any depth phases, and since this
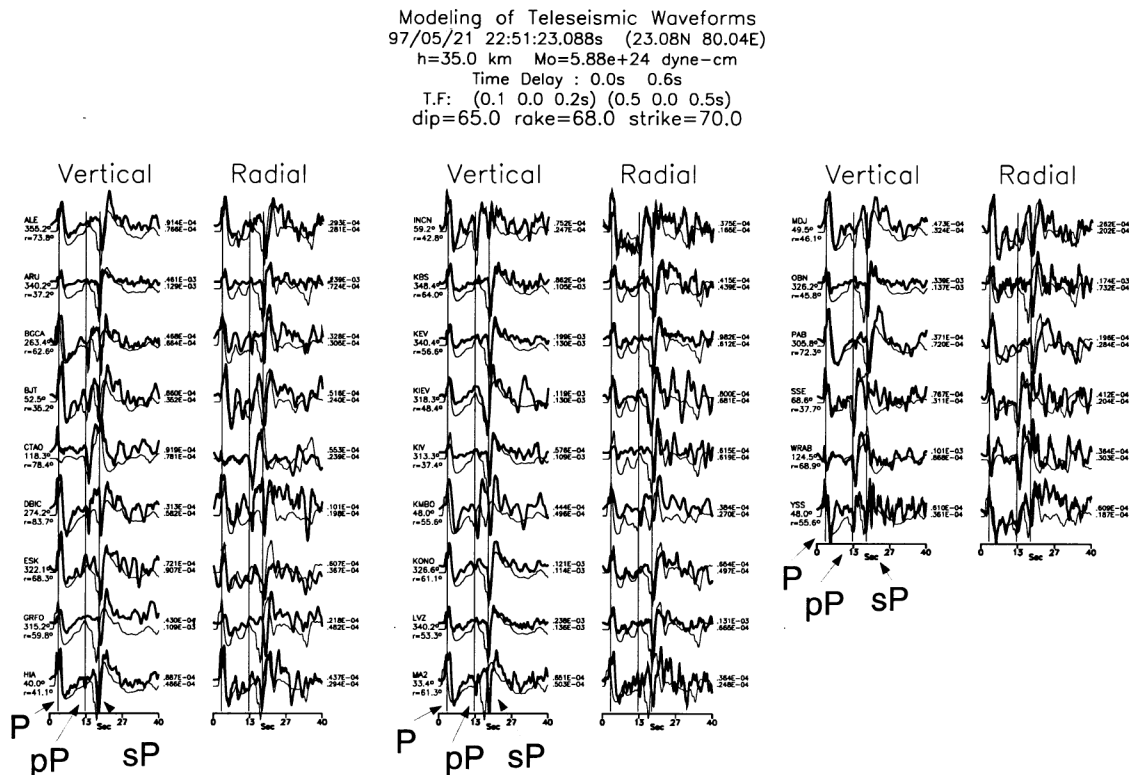
Modeling of Teleseismic Waveforms
97/05/21 22:51:23.088s (23.08N 80.04E)
h=35.0 km Mo=5.88e+24 dyne−cm
Time Delay : 0.0s 0.6s
T.F: (0.1 0.0 0.2s) (0.5 0.0 0.5s)
dip=65.0 rake=68.0 strike=70.0

Figure 2. Teleseismic modelling of vertical and radial P-wave displacement seismograms of the 21 May 1997 Jabalpur earthquake. The thick and thin lines correspond to the data and synthetic seismograms computed for a source depth of 35 km and the focal mechanism as indicated, respectively; amplitudes are plotted in 'cm'. We used two seismic sources, the second source being delayed by 0.6 s, allowing the two sources to co-locate with a seismic moment M_0 ratio of 1 (1st source) to 3 (2nd source).

feature is observed at most of the teleseismic stations, it must be a source-related phenomenon. In fact the United States Geological Survey (USGS) had pointed out the existence of these two events and estimated them to be about 1 s apart. In the subsequent investigation, Singh et al.[15] analysed the initial portion of the P_{nl} seismograms from six regional stations from the Indian National Network of Broadband Stations operated by IMD and concluded that the earthquake did, indeed, consist of two events, although a detailed modelling was not attempted to decipher the composition of these records. We synthesized these two sources using two triangular source time functions with a seismic moment ratio of 1 to 3, conserving the total seismic moment of 5.88×10^{24} dyne-cm for the earthquake. The first source has a sharp rise-time (0.1 s) compared to its 0.2 s of healing time. The second source has a total duration of 1 s with equal rise and healing time; thus the source function of the second event is longer than the source time function of the first, which is also evident in Figure 3 b. Our modelling indicated that
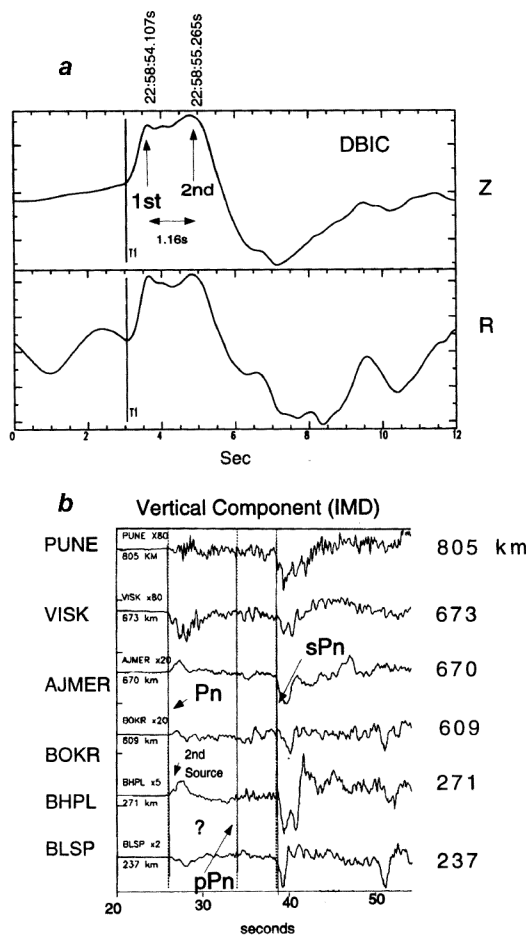

Figure 3. *a*, Observed vertical and radial *P*-wave displacement seismograms recorded at a teleseismic station DBIC ($\Delta = 83.7°$) illustrating the presence of two seismic sources, a feature which was observed at many teleseismic stations; *b*, Example of P_{nl} waves recorded by several regional stations operated by the IMD (modified from Singh et al.[15]), the depth phase sP_n showing a constant move-out from the P_n phase.

these two sources are separated by only 0.6 s. It is clear that like the teleseismic seismograms, the P_n onset is complex at the regional stations BLSP, BHPL, VISK, AJMER and PUNE, a feature that warrants further modelling to understand the source complexity and the path effect. This additional analysis is beyond the scope of this paper as we have yet to obtain access to these digital data.

The grid-search analysis of the teleseismic data yielded 35 km as the best fitting depth, one kilometre shallower than the PDE depth. A seismic moment of 5.88×10^{24} dyne-cm was obtained. The best fitting source parameters are $\delta = 65°$, $\lambda = 68°$ and $\Phi = 70°$. The parameters for the conjugate solution are δ of $32.8°$, λ of $128.8°$ and Φ of $293.7°$. The *T*, *N* and *P* axes have $63.3°$, $19.8°$ and $17.2°$ of plunge, which have azimuths of $303.9°$, $79.7°$ and $176.1°$, respectively. These values are quite similar to those determined from the first-motion *P*-wave polarities by Bhattacharya et al.[14], except for the strike which is off by $15°$. This teleseismic solution is similar to the solution reported by Singh et al.[15] which was obtained by modelling of the broadband regional seismograms from the IMD. For the Harvard centroid–moment–tensor (CMT) solution: NP1: $\delta = 26°$, $\lambda = 129°$, $\Phi = 283°$; NP2: $\delta = 70°$, $\lambda = 73°$, $\Phi = 61°$, $M_0 = 5.8 \times 10^{24}$ dyne-cm; and for the USGS broadband source parameters: NP1: $\delta = 20°$, $\lambda = 90°$, $\Phi = 255°$, and NP2: $\delta = 70°$, $\lambda = 90°$, $\Phi = 75°$, $M_0 = 2.7 \times 10^{24}$ dyne-cm. The latter moment is lower due to the assumed smaller t^* (attenuation).

Path calibration using regional seismograms

Once the depth and focal mechanism are known for a set of master events, regional seismograms can be modelled to calibrate regional structure. This is done by forward modelling of the seismograms by adjusting the crustal velocity structure to fit the waveform observations better in conjunction with other geophysical constraints, such as the established P_n velocity, Moho depth constrained by reflection or other studies, teleseismic receiver functions, and surface-wave dispersion.

To construct the regional synthetic seismogram, we used a frequency–wave number algorithm[22] based on the propagator-matrix technique[16]. The algorithm has been modified to add efficiency by using the compound matrix formulation[23] and the integral response is evaluated using Filon's quadrature[24]. The algorithm has performed better for models consisting of many layers and for responses at high frequencies than those developed based on the integration criteria of Bouchon[25]. The $F(k, \omega)$ response of a layered medium computed for a given ω and for a suite of wave numbers k is integrated as follows,

$$F(r, \omega) = \int_0^\infty F(k, \omega) k J_n(kr) \, dk. \qquad (4)$$

For evaluation of the regional wavefield, the Bessel functions are approximated by the principal asymptotic form

of the Hankel's function representation of the outgoing wavefield, thus reducing eq. (4) to

$$F(r,\omega) = \sqrt{\frac{2}{\pi r}} \int_0^\infty \sqrt{k} F(k,\omega) e^{-(kr - n\pi/2 - \pi/4)} \, dk. \qquad (5)$$

At low frequencies, wave number integrals are evaluated using the wave number sampling interval $\ddot{A}k = 2\pi/L$ where

$$\sqrt{[(L-r)^2 + h^2]} > \alpha T \qquad L > 2r, \qquad (6)$$

α, H and T being the highest velocity, the depth of the source and the length of the time series, respectively[25]. At high frequencies, the integral is evaluated advantageously using the Filon's quadrature integration scheme using a larger sampling interval[21,24]. Similarly to the teleseismic modHSKL, the frequency–wave number algorithm[22] also yields point-source time-domain wavefields for the fundamental faults for the vertical, radial and tangential seismograms. Equations (1) through (3) are used to combine these responses to generate the vertical, radial and tangential wavefields for an arbitrary fault orientation.

In this paper we concentrate primarily on the calibration of crustal structure from the source to station HYB. We have started with a regional model from Gaur and Priestley[26] which was developed based on the analysis of the teleseismic receiver function effects. They processed broadband seismograms from 11 earthquakes recorded at HYB to form the radial receiver functions which they modelled by constraining the surface layer to be 10 km thick with a shear wave velocity of 3.54 ± 0.07 km/s. This layer is underlain by a lower crust of 26 ± 1 km thickness in which the shear velocity increases to about 4.1 ± 0.05 km/s at its base, just above the Moho transition. Such gradient structures generally help in turning rays upward. We did not incorporate this detailed velocity distribution into the structure as broadband modelling of regional waveforms has no such resolution in the frequency range for which we model them; such a detailed structure becomes helpful only when modelling is done at higher frequencies. Previous experience in modelling of regional broadband seismograms in north-western Pakistan, southern California and central China, where the crustal structures are complex, suggests that a crustal structure which consists of only a few layers produces the amplitude and travel times for the majority of the seismic phases often observed from many earthquakes[1,2,4]. Based on this experience we decided to approximate the structure of the lower-crust gradient by just one layer.

The crustal model developed in this study (Table 1) produces travel times and amplitudes of P, S and surface waves in synthetic seismograms generated at HYB located at a distance of 645 km from the source that exhibit remarkable fit to the data (Figure 4). We used the same Q

values for the entire crust; Q_α (P-wave Q) and Q_β (shear-wave Q) are 1000 and 500, respectively. The vertical and radial Rayleigh waves are also modelled reasonably well. Notably, the model has also produced the correct travel times for the Love wave relative to the Rayleigh waves. The fit to the classical head wave groups (S_n, sS_n) is remarkable as can be seen in tangential seismograms, which validates the appropriateness of this model.

In general, the approach taken to develop regional waveguide begins with a relatively simple 1D model with a couple of crustal layers over a mantle half space, only incorporating additional layers to include the significant discrepancies between observed and synthetic waveforms. Generally, this is done by modifying the overall thickness of the crust and velocities of the crustal layers and the upper-most mantle. The primary upper layer, corresponding to the sedimentary structure, strongly affects the Rayleigh waves and the character of the PL (extended P-wave) and S wavetrains[21,27–29], especially at high frequencies. If the initial P wave is sharp and impulsive with the character of turning ray rather than the longer period, more ramp-like head-wave character, a detailed model with a gradient in the mantle structure needs to be used[22].
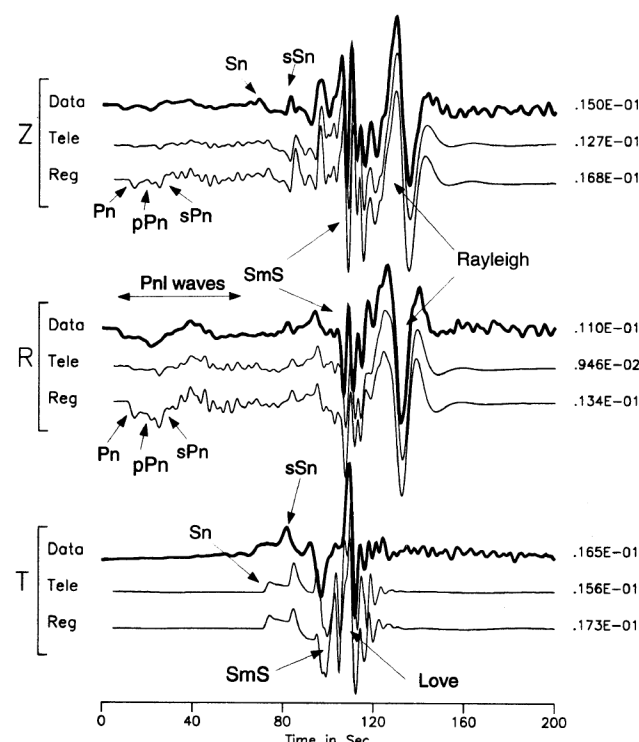
Figure 4. Regional modelling of three-component broadband seismograms recorded at station HYB (Hyderabad, India) from the 21 May 1997 Jabalpur earthquake. We compare the synthetic seismograms generated using the teleseismic focal mechanism solution (the second trace in each component) and the synthetic seismograms generated using the regional waveform focal mechanism solution (the third trace) with the recorded observations (the top thick lined seismogram), which indicates good agreement. A seismic moment of 5.9×10^{24} dyne-cm was used and amplitudes are in 'cm'.

Attenuation can also be estimated for the crustal model if source mechanisms, event depth and moments are known by matching the absolute waveform amplitude comparisons between observation and synthetics.

Regional seismogram inversion for source parameters

This section on regional modelling is presented in three phases. First, the method is reviewed, followed by the application of forward modelling of regional seismograms of the Jabalpur earthquake. Using these Green's functions we reinvert the regional data for source parameters.

Method

In this section we briefly outline a method of inverting broadband regional seismograms to retrieve reliable source parameters, assuming a well-calibrated crust. Given the observed regional seismograms $O(t)$ from an earthquake and its synthetic seismograms $S(t)$ for an arbitrary fault (δ, λ, $\ddot{O}$), we measure the misfit error, or $L1$ norm, and determine the best solution using the minimum misfit error constraint between the data and the synthetic seismograms[7]. We use a grid-search technique for all possible focal mechanisms to estimate the normalized cross-correlation functions for both P_{nl} and surface waves

separately and together. The best solution obtained based on the normalized cross-correlation functions, estimated using both P_{nl} and surface waves together, is referred to as the globally optimal solution. $S(t)$ is represented by

$$S_{W,Q}(t) = DD_{W,Q}(t)A_3 + DS_{W,Q}(t)A_2 + SS_{W,Q}(t)A_1,$$

(7)

$$S_V(t) = DS_V(t)A_5 + SS_V(t)A_4$$

where W, Q and V represent the vertical, radial and tangential wavefields, respectively; and DD, DS and SS represent the 45° dipping dip-slip, 90° dipping dip-slip and strike-slip fault, respectively.

We further express the vertical and radial normalized cross-correlation functions between the data and synthetics as

$$\frac{O(t) \otimes S(t)}{\max[\sqrt{[O(t) \otimes O(t)][S(t) \otimes S(t)]}]} =$$

$$\frac{[O(t) \otimes DD(t)]A_3 + [O(t) \otimes DS(t)]A_2 + [O(t) \otimes SS(t)]A_1}{\max[\sqrt{[O(t) \otimes O(t)][S(t) \otimes S(t)]}]},$$

(8)

where the symbol $\otimes$ represents the cross-correlation operation.

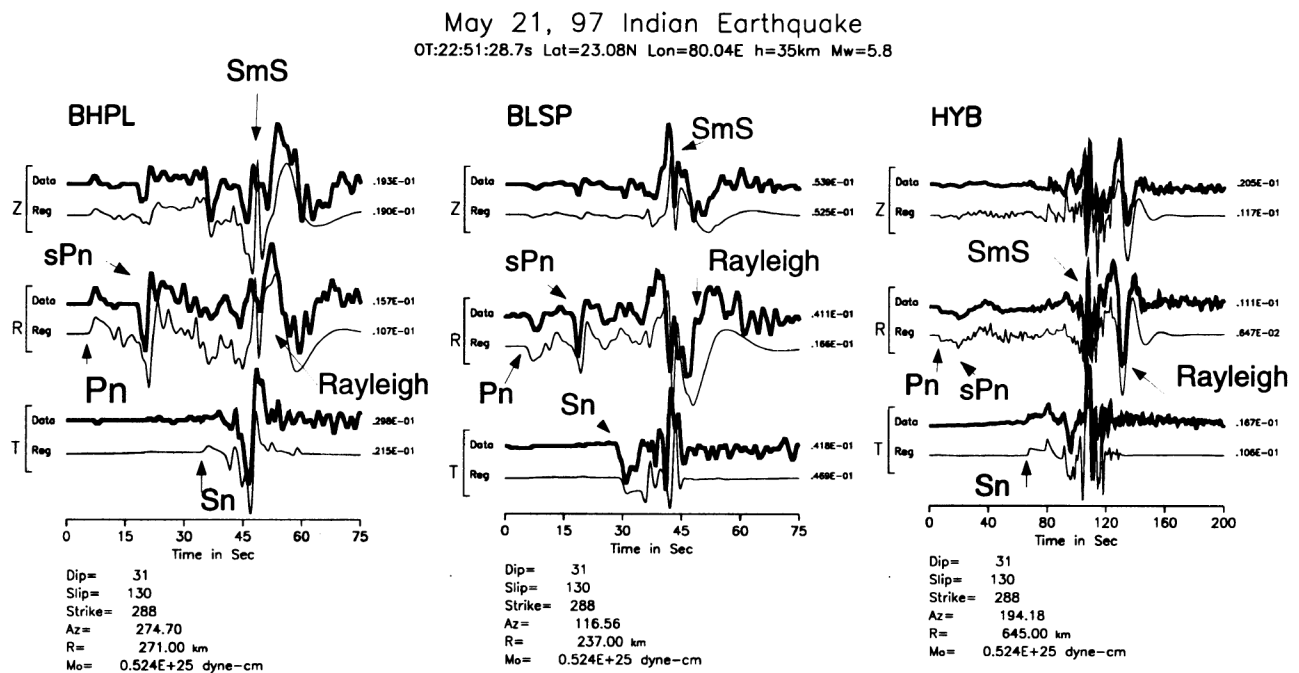**Figure 5.** Comparison between the data and the synthetic regional seismograms at stations BHPL (Bhopal), BLSP (Bilaspur) and HYB (Hyderabad). Note the agreement in travel times of sP_n, S_n, and surface waves relative to the P_n onset. The P_n onset is aligned in absolute travel times for both the data and synthetics. The regional seismograms of BHPL and BLSP were recovered from Singh et al.[15] using a hand-held digitizer.

$$S(t) \otimes S(t) = [DD(t) \otimes DD(t)]A_3A_3 + [DS(t) \otimes DS(t)]A_2A_2$$
$$+ [SS(t) \otimes SS(t)]A_1A_1$$
$$+ [DD(t) \otimes DS(t) + DS(t) \otimes DD(t)]A_3A_2$$
$$+ [SS(t) \otimes DD(t) + DD(t) \otimes SS(t)]A_1A_3$$
$$+ [DS(t) \otimes SS(t) + SS(t) \otimes DS(t)]A_2A_1 \qquad (9)$$

Each cross-correlation $\otimes$ operation on the right side of the equation is independent of the focal mechanism and can be stored before the grid search and estimated using the Fast Fourier Transforms of the time series. This makes the algorithm efficient by reducing the run time.

Often for regions with large lateral variations in the crustal waveguide, surface waves prove to be difficult to model using a single 1D crustal velocity model because the velocities in the upper crust vary from one station to another, causing the travel times of surface waves to vary. One approach to overcome this difficulty is to consider the P_{nl} and surface waves separately. There are two issues which make source estimation using the entire seismograms difficult. First, the whole-seismogram inversion can be influenced by the surface waves because of their large amplitude. Unless the event is very deep, the P_{nl} waves are relatively small; but are very useful for source estimation as they are stable and insensitive to variations in the velocity[3(a,b),27,28]. Generally, the amplitude ratio between the P_{nl} and surface waves is a good indicator of source depth. Secondly, as these two portions of the waveforms propagate through the regional waveguide differently, the calibrated velocity models must be able to accommodate these effects for both portions of the wavefield.

The path effects alone can make it difficult to fit the relative timings between the P_{nl}, S_{nl} and surface waves in tectonic provinces. Fitting the relative timings between the Rayleigh and Love waves is a difficult task. Therefore, to invert regional waveform data we use an approach[30] that separates the P_{nl} and surface waves into two

different wave groups to mitigate timing differences between the two groups in the synthetic and observed seismograms, analogous to an approach earlier used by Saikia and Herrmann[6], in which P and S waveforms of local earthquakes were inverted as two separate wave-groups using cross-correlation functions by sweeping through the focal sphere parameter space. Analysis of regional seismograms includes additional analysis of misfit errors, i.e. it uses the amplitude information[7], and is known as the cut-and-paste (CAP)[7] method which allows modelling of the P_{nl} and surface waves together but without having to worry about the relative time separations between the two types. This relaxation of timing proves to be quite useful in both regional and local earthquakes when the crustal waveguide is not perfect and initial event locations are less accurate[3(a,b),10,19]. In this method, the best solution is determined by minimizing the misfit error which is normalized by data and synthetics and does not fully utilize the amplitude information to constrain the source orientation and event depth.

To fully utilize the amplitude data, Zhu and Helmberger[10] used a distance scaling factor to normalize amplitudes in the inversion to avoid biases in the estimated source parameters introduced by the nearer observations. Both P_{nl} and surface waves are normalized to a reference distance r_0, allowing the P_{nl} waves to decay as $1/r$ and surface waves as $1/r^{1/2}$. A general expression for the misfit error e between a segment of observed $u(t)$ and synthetic $s(t)$ waveform is given by

$$e = (r/r_0)^p \| u(t) - s(t) \|,$$

where the scaling factor p is 1 for the P_{nl} waves and is 0.5 for the surface waves[10]. These scaling factors may be adjusted corresponding to the actual amplitude decay rate of these waves after a certain amount of data has been accumulated for a particular area. For the whole waveform the total misfit error is a weighted sum of the two

Table 2. Source parameters estimated by inverting regional seismograms per station and combination (values within parenthesis refer to the conjugate solution)

Station	Dip (δ) deg	Rake (λ) deg	deg	Moment, M_0 dyne-cm	M_W
HYB	33 (59.6)	68 (103.7)	188 (33.7)	0.59×10^{25}	5.8
BHPL	23 (67.5)	102 (85.0)	268 (75.0)	0.44×10^{25}	5.7
BLSP	23 (70.1)	148 (70.2)	274 (33.9)	0.47×10^{25}	5.7
BHPL + BLSP	21 (71.2)	116 (80.5)	270 (62.4)	0.47×10^{25}	5.7
All	31 (66.8)	130 (68.9)	288 (63.6)	0.58×10^{25} –	5.8 –

errors estimated for the P_{nl} and surface waves using the above expression. Since surface waves are larger in amplitude, which is usually 2 to 4 times that of the P_{nl} waves, and since P_{nl} waves are insensitive to structural variations, inversion can be weighted heavily for the P_{nl} waves to improve the source estimates. Note that because of this scaling, the relative P_{nl} and surface wave amplitude information of stations at large distances is also preserved. In general, surface waves show larger misfits compared to the misfits in body waves, as the surface waves are more affected by the lateral heterogeneity of crustal waveguides.

Application of regional inversion to Jabalpur earthquake of 21 May 1997

We also use additional regional seismograms recorded at stations BHPL (Bhopal, $R = 271$ km) and Bilaspur (BLSP, $R = 237$ km) to apply the inversion technique to demonstrate its applicability. The regional seismograms of BHPL and BLSP were investigated earlier by Singh et al.[15] in great detail, which established models along these paths (Table 1). Our aim here is to understand the various aspects of regional seismogram inversion in order to establish guidelines so that subsequent studies can be followed on the large amount of data currently archived at the National Data Centre at IMD, New Delhi. A few addi-

tional broadband stations recorded this earthquake which needs to be investigated. For this study we digitized regional seismograms for stations BHPL and BLSP directly from a published paper (figure 10 of Singh et al.[15]); these digitized data are accurate only up to 1 Hz.

We used the crustal model of HYB to compute the Green's functions for HYB station and the crustal models of Singh et al.[15] to compute the Green's functions for the other two stations. Using the same source complexity and event depth identified in the teleseismic investigation, we reprocessed a new set of Green's functions using a seismic moment partition of 1 and 3 between the two sources. Using these Green's functions, we inverted the three-component seismograms of the three stations and obtained a best-fitting focal mechanism solution similar to that of the teleseismic study. The solution obtained by inverting only the P_{nl} waves was slightly different from the full regional solution and had a dip of 37°, rake of 124° and strike of 278°, with its conjugate fault plane having a dip of 60°, rake of 67.2° and a strike of 57.8°. Figure 5 shows a comparison between data and synthetics at these stations for the global focal mechanism solution. In addition to fitting the major seismic phases (P, S and surface waves), the other phases are also remarkably fit. For this global solution we obtained a total misfit error which is very small. After scanning through the misfit errors for individual global solutions, we found a total of 22 solutions which had a total misfit error of 0.94e-04 or less, of which
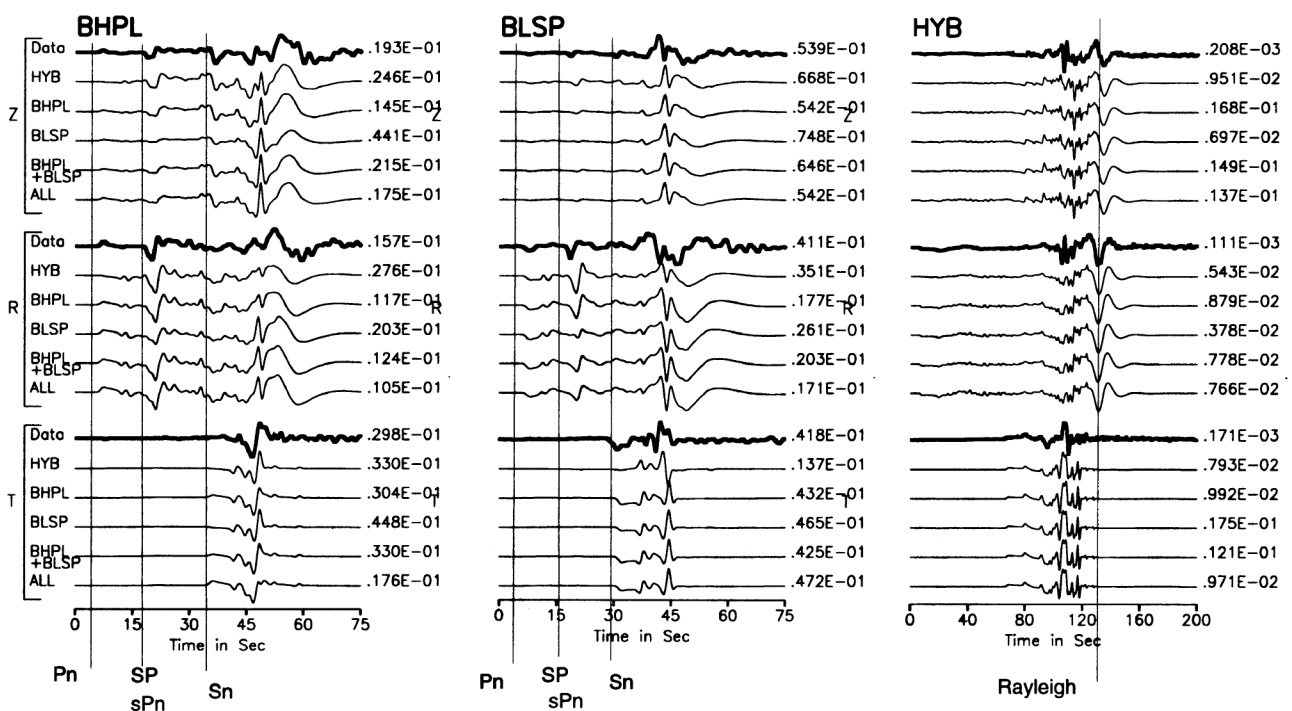
Figure 6. Illustration of regional inversion technique presented in this paper using different combination of regional seismograms from stations BHPL, BLSP and HYB. The left panel is only for the station BHPL where vertical, radial and tangential displacement synthetic seismograms are generated using various focal mechanism solutions and seismic moment (see Table 1), but the Green's functions is from the BHPL. The middle panel is for station BLSP and right panel is for the station HYB. Note that except for the solution HYB, all solutions result in similar looking synthetic seismograms. Clearly, the amplitude (cm) variation is more noticeable than the effect of the stations used in the inversion.

14 solutions had $29° \leq \ddot{a} \leq 33°$, $128° \leq \lambda \leq 132°$ and $280° \leq \phi \leq 288°$; 7 solutions had $65° \leq \ddot{a} \leq 67°$, $68° \leq \lambda \leq 72°$ and $60° \leq \phi \leq 0°$; and for one solution $\delta = 69°$, $\ddot{e} = 70°$ and $\phi = 52°$ with seismic moment ranging from 4.793×10^{24} to 6.183×10^{24} dyne-cm for the entire group.

Single vs multi-station inversion

We also determined source parameters by inverting regional seismograms of stations BHPL, BLSP and HYB separately. Regional seismograms from stations BHPL and BLSP were also inverted together because these two station locations provide a better control on the solutions. The source parameters obtained from this study are given in Table 2. Figure 6 shows a comparison of the waveforms at individual stations using the focal mechanism solutions given in Table 2. Clearly, the synthetic seismograms computed using the various solutions are quite similar and yield a reasonable fit to the data. At HYB, the P_{nl} seismograms are weak relative to the surface waves and the solution is controlled primarily by surface waves.

All inversions produced consistent estimates of the seismic moment. Stations BHPL and BLSP produced better results because of several dominant seismic phases that developed in addition to the Rayleigh and Love waves. These phases provide additional constraints for the inversion.

Up-going down-going regional waves

In this study we use the up-going and down-going seismic wavefields to investigate the composition of regional seismic phases recorded for the 21 May 1997 Jabalpur earthquake. In a recent study, Singh et al.[15] had plotted the initial 80 s of the broadband ground velocity waveforms from several regional stations and identified three head waves, namely the P_n, pP_n and sP_n phases, where the subscript n indicates that it is a head wave related to that ray. That is, sP_n is the head wave associated with the ray which leaves upwards as S wave, converts to a P wave at the free surface and arrives at the receiver after reflecting from the Moho. These phases were also identified by

Figure 7. Decomposition of recorded displacement seismograms (uppermost trace) in terms of up-going (Up) and down-going (Dn) wavefields computed using the frequency–wave number integration scheme of Saikia and Helmberger[31]. The total wavefield is shown by 'Reg'. It illustrates how the second large arrival following the P_n waves is actually produced by a simultaneous arrival of two seismic phases, namely the SP and sP_n waves, identified using generalized ray-theory seismograms; these waves are strongly seen in the 'Up' wavefield. The 'Dn' wavefield shows P_n, PmP and $PmPPmP$, including the corresponding S phases and surface waves. This kind of decomposition is helpful in separating the waveguide effects, especially the wavefield produced by the diving high-frequency body waves downward from the wavefield produced by the up-going long-period surface waves from the source.

Bhattacharya et al.[14]. Because they arrive at the same time irrespective of the epicentral distances indicates that the second major phase following the P_n wave is sP_n, which is also consistent with the travel-time analysis. However, in this study we illustrate that the composition of sP_n phase is a little more complicated at stations BHPL and BLSP, between 230 and 280 km from the source. Another phase SP, which travels to the surface as a S wave and then propagates to the receiver as a P wave along the free surface, arrives at the same time as the sP_n with a large amplitude. While this SP phase will have move-out with respect to the P_n with increased epicentral distance and may sometimes become strong, the sP_n does not have any move-out relative to the P_n and remains strong within the P_{nl} window; hence sP_n remains a good indicator of event depth out to a large epicentral distance.

To further understand the composition of SP and sP_n waves, we simulated up-going and down-going seismograms using frequency–wave number synthetics for a point source[31]. Figure 7 shows these various wavefields for the three regional stations for the vertical (Z), radial (R) and tangential (T) components. The dominant second phase, sP_n, following the P waves at BHPL is evident in both down-going (Dn) and up-going (Up) wavefields, but more strongly in the Up component. The direct P waves arrive later than the P_n waves as is evident by the first break in the Up wavefield. At BLSP it is the Dn wavefield which is stronger. For the synthetic seismograms at HYB, the arrival near the sP_n is much stronger in the Dn wavefield than in the Up wavefield. The longer-period surface waves are always strong in the Up wavefields as expected. Thus the phase which is identified as sP_n previously is indeed a composition of two wave types that separate at larger epicentral distances.

Figure 8 is a further decomposition of the Up wavefield into two components, Up$^-$ and Up$^+$, so that the interference of seismic phases becomes more evident. The Up wavefield is obtained by deleting the Moho interface from the model, i.e. the lower crust becomes itself the half space which eliminates the contribution from the Moho reflection. This Up$^-$ wavefield is numerically subtracted from the total Up wavefield to yield the Up$^+$ wavefield. Hence, the Up$^+$ wavefield should only retain the response of the sP_n waves. Note in the BHPL seismograms that Up$^-$ and Up$^+$ wavefields both have strong arrivals, which is clear on the radial seismograms at the arrival time of sP_n. Since the Up$^-$ wavefield does not include the Moho interface, the strong phase is the SP phase, which we have identified using the generalized ray theory.

Figure 9 shows a profile of vertical and radial synthetic seismograms using the same source parameters at an azimuth of 274.7°, corresponding to the station BHPL. This profile shows the sP_n phase, which has 12 s of separation from the P-onset, to have the largest amplitude on the vertical component in the distance range of 170 km to about 250 km. It is strong on the radial component to a

larger distance. However, it starts to separate from a later stronger pulse at about 300 km and becomes significantly smaller compared to the S waves and surface waves. Therefore, these waves fail to influence the inversion of regional seismograms at larger distances, which are mostly controlled by the surface waves, unless a greater weight is placed on the P_{nl} waves.

Modelling of far-regional seismograms ($\Delta = 12°$)

The Jabalpur earthquake was also recorded by several stations at far-regional distance range. Of these, we have used two stations, LSA (Lhasa, $R = 1328$ km) which is located in China and NIL (Nilore, $R = 1346$ km) which is located in Pakistan. To model these seismograms, we extended the lithospheric structure by additional 90 km into the mantle and introduced a small gradient in both P- and S-wave mantle velocities. Figure 10 shows a com-
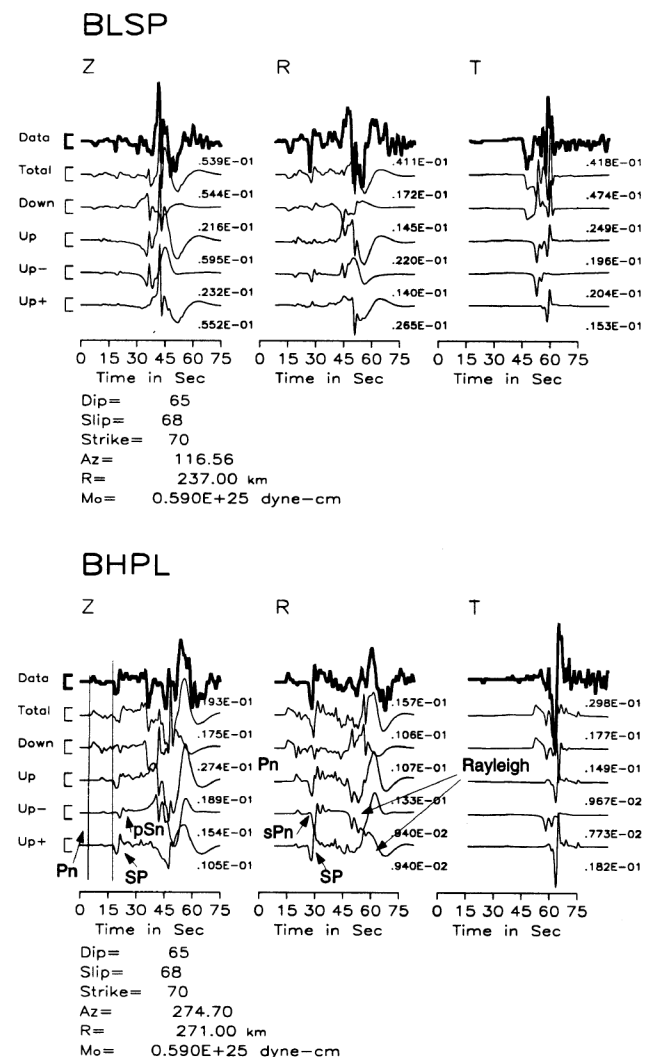

BLSP

Z   R   T

Data
Total   .539E-01   .411E-01   .418E-01
Down   .544E-01   .172E-01   .474E-01
Up   .216E-01   .145E-01   .249E-01
Up−   .595E-01   .220E-01   .196E-01
Up+   .232E-01   .140E-01   .204E-01
            .552E-01   .265E-01   .153E-01

0 15 30 45 60 75   0 15 30 45 60 75   0 15 30 45 60 75
Time in Sec   Time in Sec   Time in Sec

Dip=   65
Slip=   68
Strike=   70
Az=   116.56
R=   237.00 km
Mo=   0.590E+25 dyne−cm

BHPL

Z   R   T

Data
Total   .93E-01   .157E-01   .298E-01
Down   .175E-01   .106E-01   .177E-01
Up   .274E-01 Pn .107E-01 Rayleigh .149E-01
Up−   .189E-01   .133E-01   .967E-02
Up+ pSn   .154E-01 sPn   .940E-02   .773E-02
Pn   SP   .105E-01   SP .940E-02   .182E-01

0 15 30 45 60 75   0 15 30 45 60 75   0 15 30 45 60 75
Time in Sec   Time in Sec   Time in Sec

Dip=   65
Slip=   68
Strike=   70
Az=   274.70
R=   271.00 km
Mo=   0.590E+25 dyne−cm

Figure 8. Further decomposition the 'Up' wavefield to separate the sP_n (Up$^-$) from the $sPmP_n$ (Up$^+$) phase. (See caption of Figure 7 for the details).

parison between data and frequency–wave number synthetics generated using the same source parameters, seismic moment and source complexity, derived from the teleseismic and regional waveform modelling. The synthetic seismograms at station LSA are consistent with the recorded seismograms both in travel times and amplitudes of various phases in the entire waveform, in addition to the high-quality agreement in the P_{nl} waves shown by displaying the initial portions of the vertical and radial components beneath the full seismograms. The P_n and sP_n waves are strong and do not appear as long-period ramp-like pulses, a feature typical of the classical head waves. Since they appear as impulse responses, they are, in fact, the rays turned by the gradient in the P velocity in the upper mantle. The sharpness in the P onset at station NIL is an indication that the structure under this station can accommodate a larger gradient than that we have introduced here. Along this path to the station NIL, the Rayleigh waves are slower than the observations, thus suggesting a lower shear velocity in the upper crust; this is currently under investigation.

Discussions

We have successfully demonstrated an approach to calibrate regional crustal structure. The method requires

earthquakes large enough to be recorded at teleseismic distances, but small enough so that the source process is not too complex. The teleseismic recordings are used to constrain depth by modelling the travel times of pP and sP phases relative to the P-wave onset, and determine focal mechanism by fitting absolute amplitude and polarity of these phases using the grid-search technique.

The 21 May 1997 Jabalpur earthquake, which occurred in central India within the stable peninsular region of the country, provided a set of high-quality data to test our regional path calibration and focal mechanism determination method. The crustal structure of this region is, in general, simple as discussed in this paper. The high quality fit for the P_n, sP_n, S_n, SmS and surface waves of the synthetic seismograms to the observed seismograms at HYB, BHPL and BLSP required a model which consisted of only two layers over a half space (Figure 4). The teleseismic P, pP and sP phases also produced excellent agreement. The mismatch in the finer detail of the seismograms can be improved by adding separate receiver structure to each station, but such efforts are not likely to alter the inferred solutions.

The regional calibration follows after the depth and focal mechanisms of the master events have been established. In this paper, we illustrated the use of a set of algorithms which are used for constructing teleseismic
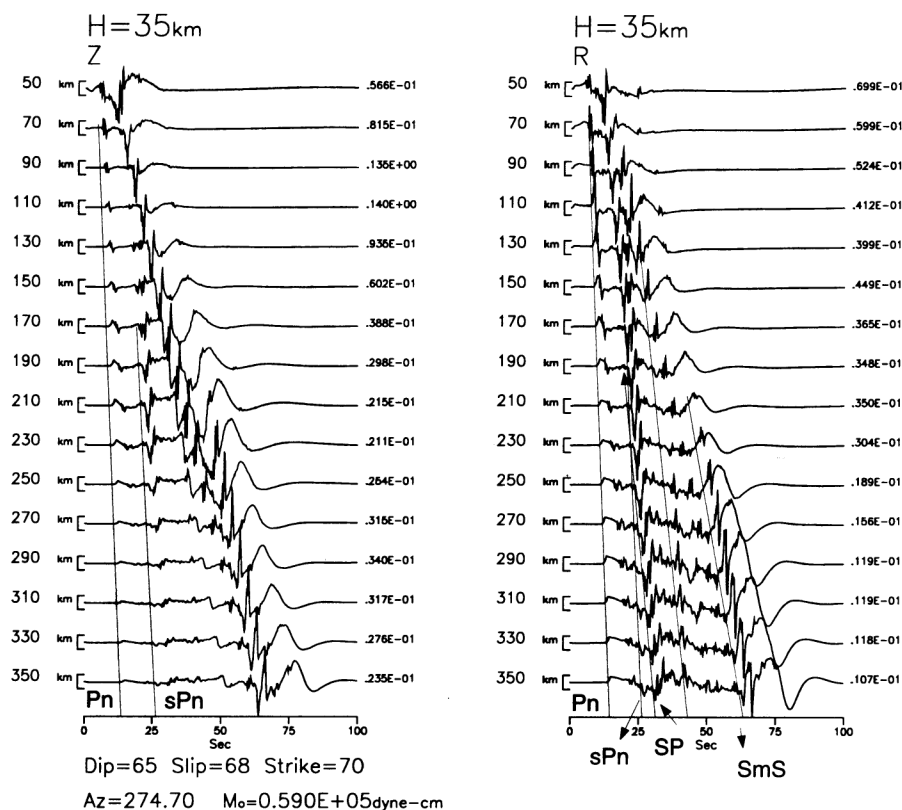

Figure 9. Vertical and radial profiles of synthetic displacement seismograms showing the propagational evolution of regional seismic phases across the crustal structure of peninsular India.

and regional Green's function using propagator-matrix techniques[16]. These algorithms are used in conjunction with observed seismograms to invert for the focal mechanism and depth, and will be made available for use by others.

Using a simplified version of the crustal structure based on the model of Gaur and Priestley[26], we developed a model consisting of only two crustal layers underlain by a half space with P- and S-wave velocities of 8.05 km/s 4.68 km/s, respectively. The P and S velocities for the surface layer are 6.15 km/s and 3.5 km/s, respectively, and the layer has a thickness of 15 km. The lower crust is 21 km thick and has P and S velocities of 6.75 km/s and 3.85 km/s, respectively. Note that the refined regional path model to HYB is different from Gaur and Priestley's model[26] in that it does not include the Moho transition zone which they constrained to have a 4 km thickness with a shear-wave velocity of 4.74 ± 0.1 km/s. The reason for this difference is that in the receiver-function analysis the seismic wavefield impinged at the base of the station crust from the mantle steeply; thus the in-coming seismic waves traversed through a small area beneath the station. On the other hand, regional wavefields from dis within 12° propagate through by sampling a larger portion of the crust, which can also be complex in tectonic areas. Thus, while the receiver-function structures yield better fit to the teleseismic waveforms, they can often lack the features recorded in the regional seismograms. Our previous experience in central China using receiver-function structure of station WMQ[12] (a Chinese broadband station) had

also led to the same conclusion. Similarly for the Basin and Range region[27], a simple two-layered model proved sufficient to match recorded seismograms. The crustal structure model for station HYB, used in this study, is primarily based on our prior experiences in which we successfully modelled broadband regional seismograms at station HRV (Harvard) from the Saguenay earthquake of 25 November 1988 in Quebec, Canada which was recorded at 640 km away in United States (see figure 5 of Saikia[22]). The regional seismograms at HYB and HRV look similar in the P_{nl} amplitude relative to the surface waves and both events occurred in the lower crust with a similar source complexity. But unlike in the case of the Quebec earthquake for the path to station HRV, the path to HYB from the Jabalpur earthquake does not warrant any gradient to fit the characteristics recorded in these broadband seismograms.

By modelling regional seismograms we have shown that regional P_n and sP_n phases can be used to establish the source depth. The other regional depth-related phase, pP_n, was not strong. The most interesting property of the sP_n and pP_n phases is that they do not have to move out relative to the P_n waves and so the travel-time differences $sP_n - P_n$ and $pP_n - P_n$ can become good indicators of event depth. However, there can be a problem when P_n remains in the noise level, thus making it difficult to identify.

Another important aspect of the Jabalpur earthquake analysis is that we established one solution, including its rupture complexity, which successfully fits data at all
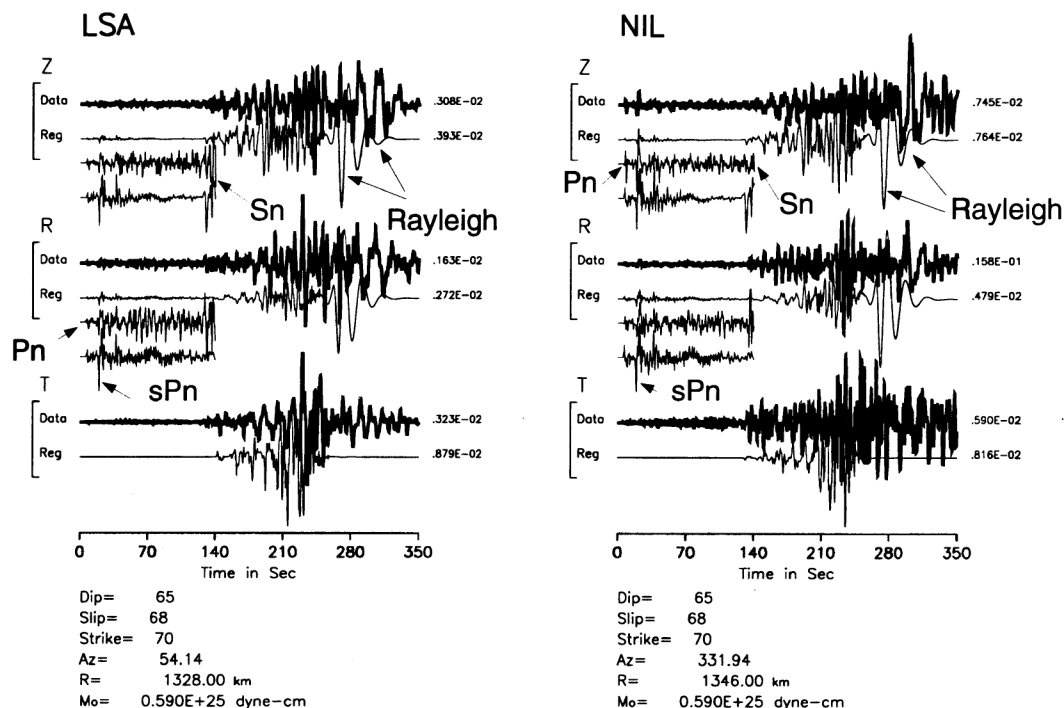

LSA

Dip=	65
Slip=	68
Strike=	70
Az=	54.14
R=	1328.00 km
Mo=	0.590E+25 dyne–cm

NIL

Dip=	65
Slip=	68
Strike=	70
Az=	331.94
R=	1346.00 km
Mo=	0.590E+25 dyne–cm

Figure 10. Modelling of far-regional seismograms recorded at stations LSA and NIL. The fit to the P_{nl} waves is reasonable at both stations, suggesting the adequacy of the upper-mantle P-wave model for the region.

ranges up to 13°, regionally and between 30° and 90°, teleseismically. Previous studies were confined to either regional analysis[15] which did not include the HYB seismograms or to teleseismic data (Harvard CMT or USGS CMT solution).

To be successful in applying this method for understanding regional seismograms recorded by the broadband stations of the IMD network from earthquakes in the northern Himalaya, Hindu Kush and eastern India, it will be necessary to examine observations carefully. We expect seismograms to look different from the ones shown here for the majority of the earthquakes with seismic paths that traverse through the Gangetic sedimentary basin of the northern India and Bengal basin of eastern India. While the early portion of the P_{nl} waves is most likely to remain stable because of their propagation path, the surface waves will exhibit strong dispersion with amplitudes likely to have a depth dependence. Our proposed method will still be able to handle such situations, but the key element for this success is obtaining a reasonable representation of the regional path crustal structure.

There are other important aspects of the regional modelling related to the problem of seismic event location, especially of small magnitude events (M_W < 5) which are observed with good signal-to-noise ratio only within regional distances, for which developing an accurate regional waveguide model is very critical. With established regionalized earth models, travel-time corrections relative to a reference model can be estimated based on accurately known event locations and these station corrections can be used in locating other events. It is important that travel-time tables are regionalized in order to determine accurate depths and locations which help reduce the model errors which are often the sources of location errors.

In addition, the existing broadband network does cover north-east India which in the last one hundred years has experienced several large earthquakes ($M_W \geq 7$), including those of 12 June 1897, $M_s \approx 8.5$; and 15 August 1950, $M_s \approx 8.7$ (ref. 32). Earthquakes in the magnitude range, $M_W \leq 5$, often occur in this region and are probably associated with faults which have been delineated from the occurrences of the modern-day seismicity, that lie under urban region, but have not been mapped geologically[33]. Modelling of regional broadband seismograms can help to relate the source parameters of these events to tectonic features, which can be determined if such data become available even from a single station. Inversion of seismograms using single-station seismograms is a common practice in retrieving source parameters of small crustal earthquakes. Small earthquakes ($M_W \leq 4.5$) do not have CMT solutions, and often depths are unconstrained. Therefore, it is essential to have some reliability check on the solutions that are obtained in a new region from several regional observations. Previous studies in the Hindu Kush region of the Pamir Himalaya have shown that it is possible to obtain reliable solutions for such earthquakes

based on only a few regional seismograms, if the crustal structure is well calibrated[1,2,4]. Figure 11 is an example from the Pamir–Hindu Kush region illustrating that inversion using regional seismograms from two stations yields depth estimates (shown by thin lines) which are similar to those obtained by inverting regional seismograms from many stations (shown by thick lines) from the PAKN and KNET networks. The PAKN network operated temporarily in Pakistan near Nilore and the KNET is a permanent network which operates in Kyrghystan. The depth of an event is determined by minimizing the misfit error function, and in this case both the thin and thick lines have similar locations, where their misfit errors are at a minimum. The left panel in Figure 11 shows the results obtained for five shallow earthquakes and the right panel shows the results for five deep earthquakes. For the shallow earthquakes solutions are stable, even over a large range of depth, and have well-defined waveform misfit errors. A salient point is that the two inversions have produced similar source depths which are notably shallower
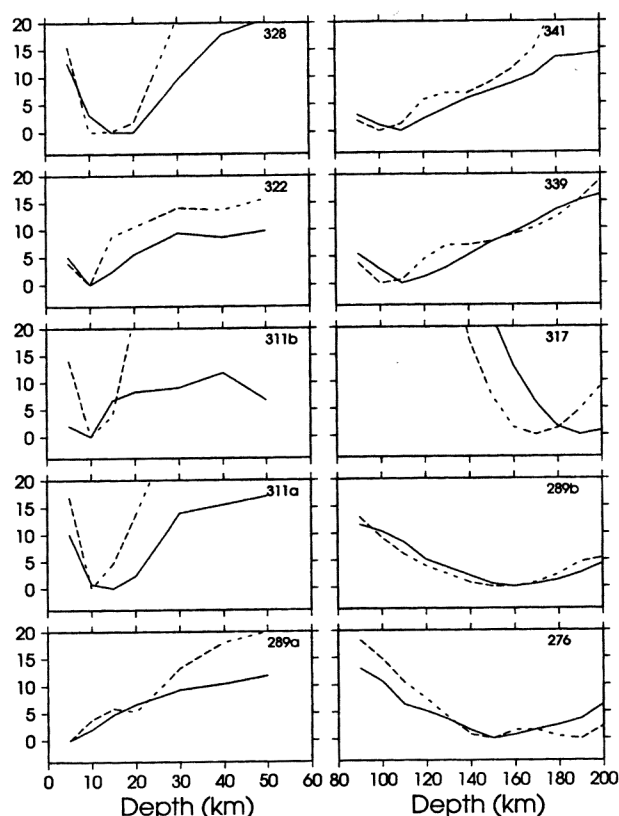

Figure 11. Depth resolution, or error-misfit curves for a set of Pamir–Hindu Kush earthquakes. The solid lines represent the case when the solutions are determined using many stations (all available stations from a temporary broadband PAKN network in Pakistan and the permanent broadband KNET network in Kyrghystan) and the thin lines represent the solutions determined using only two stations (one from the PAKN network and other from the KNET network). The left panel shows solutions for five shallow events and right panel shows solutions for five mantle events. Note both sets of solutions have similar depths where depth error misfit measures are at a minimum[9,18].
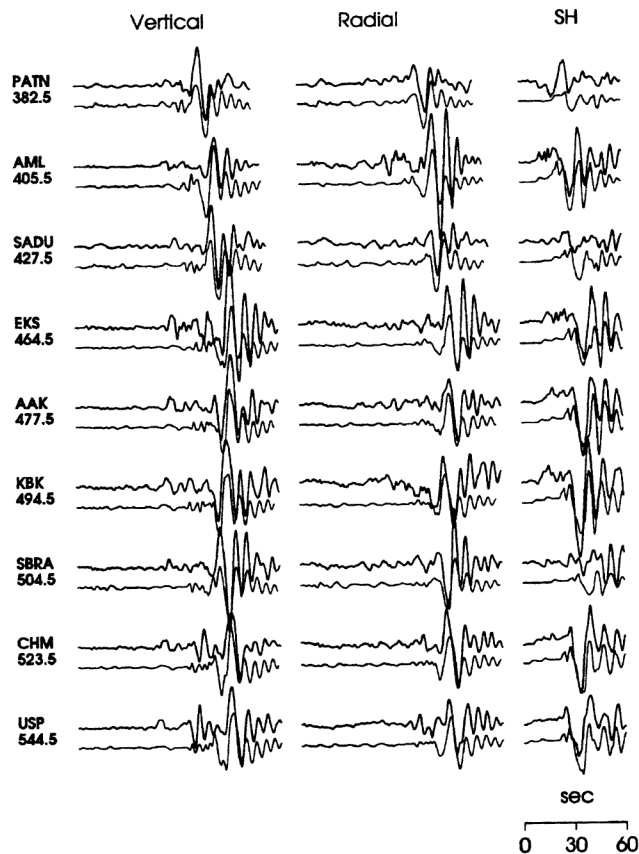
Figure 12. Comparison between data and synthetic displacement seismograms for one shallow Pamir–Hindu Kush earthquake ($\delta = 45°$, $\lambda = -35°$, and $\phi = 200°$, and depth = 15 km). For each station, the synthetic seismograms are plotted beneath the observed seismograms; displacement is in 'cm'.

than the depths in the ISC bulletin. Figure 12 shows agreement between data and synthetics for two earth-quakes, one shallow and one deep, for the depths obtained in this study[2,4]; illustrating the usefulness of the operation of broadband stations as few as two.

Establishing the various facets of regional path effects is essential toward understanding how seismic waves are amplified as they propagate through varying crustal struc-tures. These factors need to be accounted for when evalu-ating seismic hazards for various urban centres. By knowing these effects, it is easier to incorporate them in estimating the actual levels of ground motions that could be expected during large earthquakes.

1. Saikia, C. K., Woods, B. B., Thio, H. K., Zhu, L. and Helmberger, D. V., PL-TR-96-2069, Scientific Report No 1, Phillips Labora-tory, HAFB, MA, 1996, pp. 1–130.
2. Saikia, C. K., Thio, H. K., Woods, B. B., Song, X., Zhu, L. and Helmberger, D. V., PL-TR-96-2307, Scientific Report No 2, Phil-lips Laboratory, HAFB, MA, 1996, pp. 1–205.
3a. Zhao, L. -S. and Helmberger, D. V., *Geophys. Res. Lett.*, 1991, **18**, 2205–2208.
3b. Zhao, L. -S. and Helmberger, D. V., *Geophys. J. Int.*, 1991, **105**, 301–312.
4. Zhu, L., Helmberger, D. V., Saikia, C. K. and Woods, B. B., *J. Geophys. Res.*, 1997, **102**, 22,799–33,813.
5. Langston, C. A. and Helmberger, D. V., *Geophys. J. R. Astron. Soc.*, 1975, **42**, 117–130.
6. Saikia, C. K. and Hermann, R. B., *Bull. Seismol. Soc. Am.*, 1985, **75**, 1021–1041.
7. Zhao, L. -S. and Helmberger, D. V., *Bull. Seismol. Soc. Am.*, 1994, **84**, 91–94.
8. Dreger, D. S. and Helmberger D. V., *J. Geophys. Res.*, 1973, **98**, 8107–8126.
9. Saikia, C. K. and Helmberger, D. V., Final Report to Phillips Laboratory, Kirtland Air Force Base, New Mexico, Contract No F29601-91-C-DB01, 1993.
10. Zhu, L. and Helmberger, D. V., *Bull. Seismol. Soc. Am.*, 1996, **86**, 1634–1641.
11. Thio, H-K., Song, X., Saikia, C. K., Helmberger, D. V. and Woods, B. B., *J. Geophys. Res.*, 1999, **104**, 845–861.
12. Woods, B. B., Saikia, C. K., Thio, H. K. and Patton, H. J., Techni-cal Report, DoE SUB/F53310018/8f, Pasadena, CA, 1998.
13. Bondar, I., Technical Report CMR-98/21, Center of Monitoring Zresearch, Alexandria, VA, 1998.
14. Bhattacharya, S. N., Ghose, A. K., Suresh, G., Baidya, P. R. and Saxena, R. C., *Curr. Sci.*, 1997, **73**, 855–863.
15. Singh, S. K., Dattatrayam, R. S., Shapiro, N. M., Mandal, P., Pacheco, J. F. and Midha, R. K., *Bull. Seismol. Soc. Am.*, 1999, **89**, 1631–1641.
16a. Haskell, N. A., *Bull. Seismol. Soc. Am.*, 1964, **54**, 377–393.
16b. Haskell, N. A., *J. Geophys. Res.*, 1962, **67**, 4751–4767.
16c. Hudson, J. A., *Geophys. J. R. Astron. Soc.*, 1969, **18**, 233–249.
17. Ben-Menahem, A., Smith, S. W. and Teng, T., *Bull. Seismol. Soc. Am.*, 1965, **55**, 203–235.
18. Teng, T. and Ben-Menahem, A., *J. Geophys. Res.*, 1962, **70**, 5157–5170.
19. Saikia, C. K., Woods, B. B. and Thio, H. K., *Pure Appl. Geophys.*, 2000.
20. Wallace, T. C., Helmberger, D. V. and Mellman, G. R., *J. Geo-phys. Res.*, 1981, **86**, 1679–1685.
21. Wadia, D. N., *Geology of India*, Macmillan, New York, 1996.
22. Saikia, C. K., *Geophys. J. Int.*, 1994, **118**, 142–158.
23. Dunkin, J. W., *Bull. Seismol. Soc. Am.*, 1965, **55**, 335–358.
24. Frazer, L. N., Ph D thesis, Princeton University, Princeton, NJ, 1977.
25. Bouchon, M., *Bull. Seismol. Soc. Am.*, 1981, **71**, 959–971.
26. Gaur, V. K. and Priestley. K. F., *Proc. Indian Acad. Sci. (Earth Planet. Sci.)*, 1997, **106**, 1–8.
27. Song, X. J., Helmberger, D. V. and Zhao, L., *Geophys. J. Int.* 1996, **125**, 15–29.
28. Saikia, C. K. and Burdick, L. J., *J. Geophys. Res.*, 1991, **96**, 14,383–14,401.
29. Helmberger, D. V. and Engen, G. R., *Bull. Seismol. Soc. Am.* 1980, **70**, 1699–1714.
30. Zhao, L. -S. and Helmberger, D. V., *Phys. Earth Planet. Int.*, 1992, **78**, 69–95.
31. Saikia, C. K. and Helmberger, D. V., *Bull. Seismol. Soc. Am.*, 1997, **87**, 987–998.
32. Richter, C. F., *Elementary Seismology*, W.H. Freemann and Com-pany, San Francisco, 1958, p. 768.
33. Saikia, C. K. and Somerville, P. G., *J. Geophys.*, 1998, **XIX**, 35–52.